Electronic Supplementary Information

From garish to practical: synergetic effect of short-circuiting and charge-trapping for high-entropy energy harvesting

Jihong Shi,[‡a] Xiangyang Zhang,[‡a] Weilu Li,[a] Xiangkun Bo,[a] Jasim M. Almardi,[a] Zehua Peng,[a] Wen Jung Li,[a] Zhong Lin Wang,[*bc] and Walid A. Daoud,[*ad]

[a] Department of Mechanical Engineering, City University of Hong Kong, Hong Kong, China.
[b] CAS Center for Excellence in Nanoscience, Beijing Key Laboratory of Micro-nano Energy and Sensor, Beijing Institute of Nanoenergy and Nanosystems, Chinese Academy of Sciences, Beijing, China.
c School of Materials Science and Engineering, Georgia Institute of Technology, Atlanta, GA, USA.
[d] Shenzhen Research Institute, City University of Hong Kong, Shenzhen, China.

Email: wdaoud@cityu.edu.hk and zhong.wang@mse.gatech.edu

The file includes:

Figure S12. Capacitor and battery charging curve with the traditional circuit design under 300 rpm of rotation speed.

Figure S13. SEM images of Mn_3O_4 nanoparticles-loaded titanium mesh with the resolution of 50, 10 and 0.5 μm.

Figure S14. Photograph of the commercial lithium battery.

Figure S15. Photograph of the wastewater treatment system.

Video S1. Capacitor charge with wind energy.

Video S2. Battery charge with wind energy.

Video S3. Capacitor charge with water flow energy.

Video S4. Battery charge with water flow energy.

Note S1. Output analysis of a contact-separation TENG

Intrinsic characteristics of transferred charge quantity (Q_{SC}) of contact-separation TENG is given as:[1]

$$Q_{sc} = \frac{S\sigma x_{(t)}}{d_0 + x_{(t)}}$$

Where S, σ, d_0 and $x_{(t)}$ represent the surface of triboelectric layer, surface charge density, effective dielectric thickness, and the distance between the triboelectric layers, respectively. The correlation between transferred charge quantity and total triboelectric charge can be derived by dividing the numerator and denominator by $x_{(t)}$:

$$\frac{Q_{sc}}{S\sigma} = \frac{1}{\frac{d_0}{x_{(t)}} + 1}$$

Which is less than unity, indicating reduced transferred charge.

Note S2. Multiphysics simulation parameters

In using the COMOSOL simulations to analyze the potential distribution of HEEH, we applied Gauss's law (integral form):

$$\int \partial V \ dA(n.E) = \frac{1}{\varepsilon_0 \varepsilon_r} \int V \ dV\rho \quad (1)$$

we have the following assumption:

1. The triboelectrification area is infinitely large because the size of the triboelectrification layer and electrode layer is substantially larger than their thickness.
2. The inner electric field inner is uniform.

For the raw device, we have the following:

$$\int top \ dxdyz.zE(z) + \int bottom \ dxdy(-z).(-zE(z)) = \frac{1}{\varepsilon_0} \int V \ dV\rho \quad (2)$$

$$EA_{top} + EA_{bottom} = 2E(z)A = \frac{1}{\varepsilon_0} \int V \ dV\rho \quad (3)$$

$$2EA = \frac{1}{\varepsilon_0} \int V \ dV\rho \quad (4)$$

The only charge present is σ, so

$$E = \frac{\sigma}{2\varepsilon_0} \quad (5)$$

When the two triboelectrification layers are in contact, the charge present on their surface are σ_+ and σ_-, and $\sigma_+ + \sigma_- = \sigma$. Thus, there is an electrical potential (V) when there is a deplanement field (d) between the two triboelectrification layers:

$$V = \frac{\sigma}{\varepsilon_0} d \quad (6)$$

After introducing the charge trapping effect, the optimized electrical potential results from the increased dielectric constant can be expressed as:

$$V = \frac{\sigma'}{\varepsilon_0 \varepsilon_r} d \quad (7)$$

Where σ' *and* ε_r present the enhanced surface charge density and the dielectric constant of PI, and the increase of σ' outperform the ε_r, then cause the increase surface potential. With the introduction of short-circuiting effect, the electrical potential is the same as equation 7, but it would be reduced to the same level of bottom electrodes due to the extra charge flow once the short-circuiting effect is triggered.

Note S3. Measurement of the charge decay process of HEEH with CT effect

HEEH was first run for 10 minutes at a rotation speed of 150 rpm. After then, the HEEH's operating mode needs to be switched from rotation to contact-separation in order to detect the process of surface charge decay. To replace the top friction layer, another aluminum layer 3*3 cm^2 attached to the PMMA substrate was employed. To avoid the impact of excess triboelectrification charge, the spacing between two pieces was fixed at 1 mm to 10 mm during the contact-separation procedure. The contact-separation motion frequency was 1 Hz, and the experiment lasted 1000 seconds.

Note S4. Theoretical analysis of the impact of short-circuiting and charge-trapping effects on device output

The design of HEEH can be regarded as a sliding-mode freestanding triboelectric nanogenerator (*1*). The device has inherent capacitive behavior when applying the classical node concept to analyze its working principle. The capacitance of HEEH comprises two parts. First is the parasitic capacitance of two bottom electrodes, which can be neglected to simplify analysis. Second is the serial connection of the capacitance between the top friction layer and electrode 1 (C_1) and the top friction layer and electrode 2 (C_2). If we set the length of the top layer to *l* and the gap of the two bottom electrodes to *g*, and assume a small region of dk in the top friction layer (the distance of this region to the left edge of the bottom electrode is k) contains the tribo-charges with a density of σ, and correspondingly the charge quantity on bottom electrode 1 and electrode 2 varies in the range of 0 to σ*dk*. The total charges on the two bottom electrodes are:

$$Q_1 = \sigma \int_0^l \frac{dk}{1 + C_2(k)/C_1(k)} \quad (8)$$

$$Q_2 = \sigma \int_0^l \frac{dk}{1 + C_1(k)/C_2(k)} \quad (9)$$

Where $C_i(k)$ states for the capacitance between the small surface *dk* and bottom electrode *i*.

Without considering the short-circuiting effect, the transferred charges have a saturation trend as the top friction material (aluminum) moves from exactly the top of electrode 1 to electrode 2. Therefore, the transferred charge quantity Q_{tr1} and open-circuit voltage can be shown as:

$$Q_{tr1} = \int_0^l \frac{\sigma dk}{1 + (C_2(k)/C_1(k))_{x=g+l}} - \int_0^l \frac{\sigma dk}{1 + C_1(k)/C_2(k)_{x=0}} \quad (10)$$

$$V_{oc1} = \frac{\sigma x}{\varepsilon} \quad (11)$$

The Q_{tr1} and V_{oc1} are equal to the actual transferred charge quantity for our base device with neither charge-trapping nor short-circuiting effects. With the introduction of the charge-trapping effect, the surface charge density σ would be increased, resulting in the enhanced Q_{tr1} and V_{oc1} during measurement.

After introducing the short-circuiting effect, however, the charge on the surface of the top friction layer can redistribute to both the bottom electrodes to keep the same electrical potential level, which will lead to a huge disturbance of the electrostatic field distribution. Nevertheless, the redistribution of charge can barely cause a significant change of V_{oc} due to the total charge quantity for the whole device is constant, and only the period of short-circuiting contact can lead to the same potential state for the friction layer and bottom electrodes, which can be virtually observed as the zero voltage during measurement.

If the top friction layer and one of the bottom electrodes are connected to create the short-circuiting effect, the transferred charge quantity Q_{tr2} between them is:

$$Q_{tr2} = \int_0^l \frac{\sigma dk}{1 + C'_{x = position\ of\ SC\ effect}} \quad (12)$$

Where C' indicates the capacitance ratio between two parts (top friction later and one of the bottom electrodes) for creating the short-circuiting effect.

Therefore, the final Q_{tr} after introducing the short-circuiting effect is:

$$Q_{tr} = \int_0^l \frac{\sigma dk}{1 + (C_2(k)/C_1(k))_{x = g + l}} - \int_0^l \frac{\sigma dk}{1 + C_1(k)/C_2(k)_{x = 0}} + \int_0^l \frac{\sigma dk}{1 + C'_{x = position\ of\ SC\ effect}} \quad (13)$$

Comparing to Q_{tr1}, when the device is into the short-circuiting effect, the Q_{tr} can be increased due to the extra contribution of charge flow between friction layer and bottom electrodes.

Note S5. Estimations for calculating power density

1. If no thickness of acrylic substrate, PCB board, and metal electrode are provided, it is estimated at 3 mm, 1.6 mm, and 0.025 mm, respectively.
2. The thickness increment result from polyester fur is 0.03 mm[7], according to the photograph and schematic.
3. The round hole in the middle for assembling the device is considered a part of the overall area/volume.

Note S6. Parameter-setting for circuit simulation

LTspice was used to evaluate circuit functions and component sizing before circuit fabrication. To simulate the circuit performance, a TENG source was fabricated using a sine voltage source module with adjusted parameters of amplitude (370 V), frequency (240 Hz), and series resistance (100 MΩ). The diodes, J-FET switch, capacitors, and resistors are packaged modules in LTspice. Parameters, such as breakdown voltage, forward current rating, capacitance, and resistance, were adjusted for component sizing. The voltage was displayed on the scope module and exported in the workspace of LTspice.

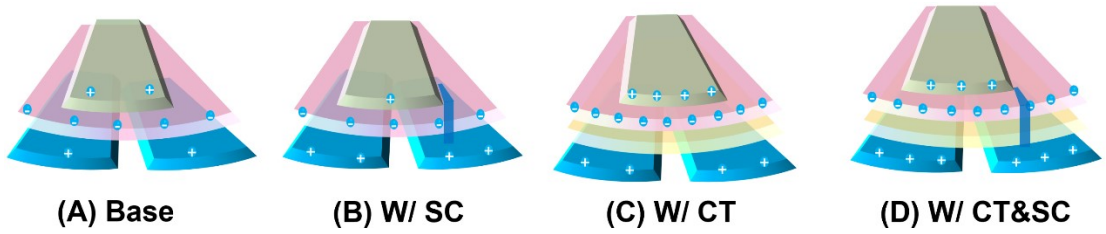

Figure. S1. Schematic illustration of the triboelectrification of base, SC, CT, and CT&SC devices.

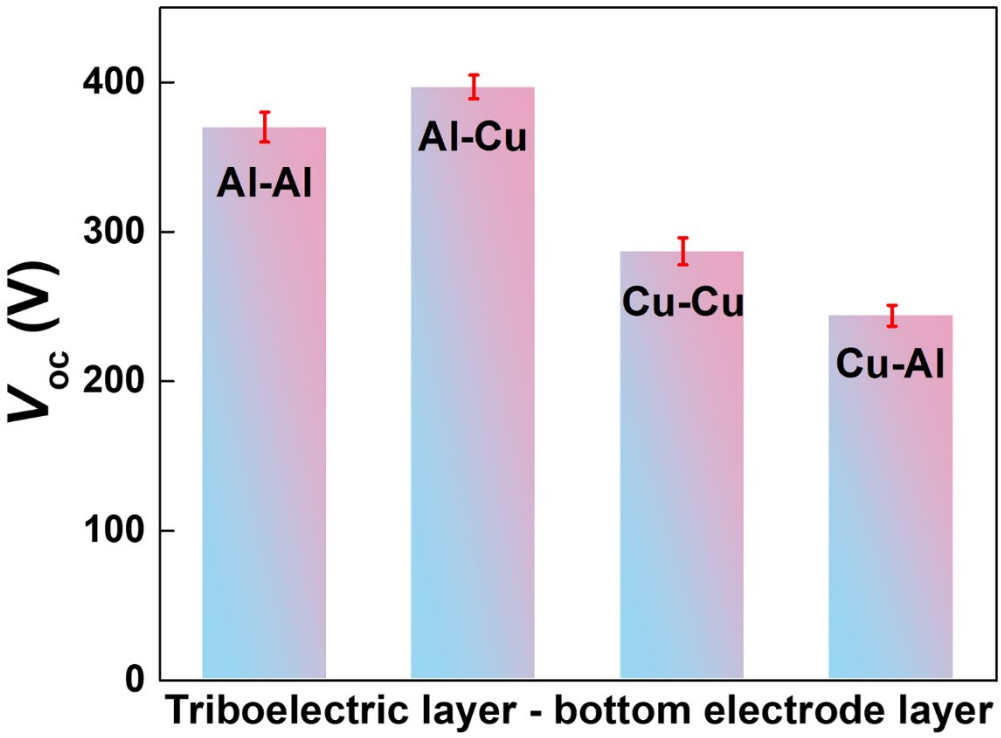

Figure. S2. Voltage output of HEEH made of different triboelectric and bottom electrode materials.

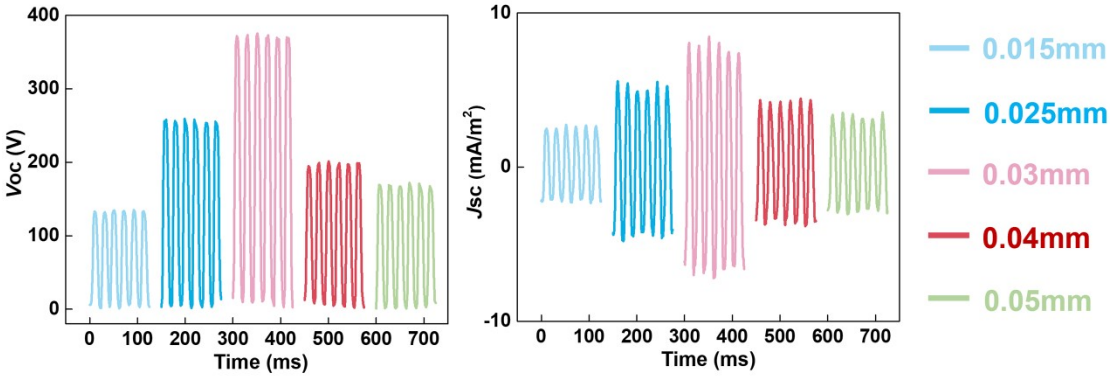

Figure. S3. Electrical outputs at different thicknesses of charge trapping layer.

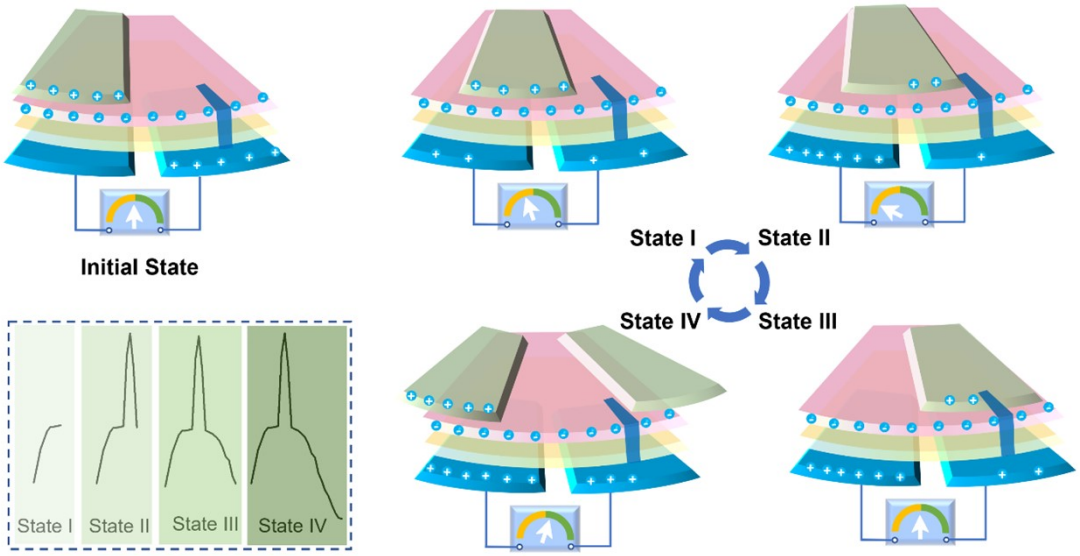

Figure. S4. Working mechanism of HEEH.

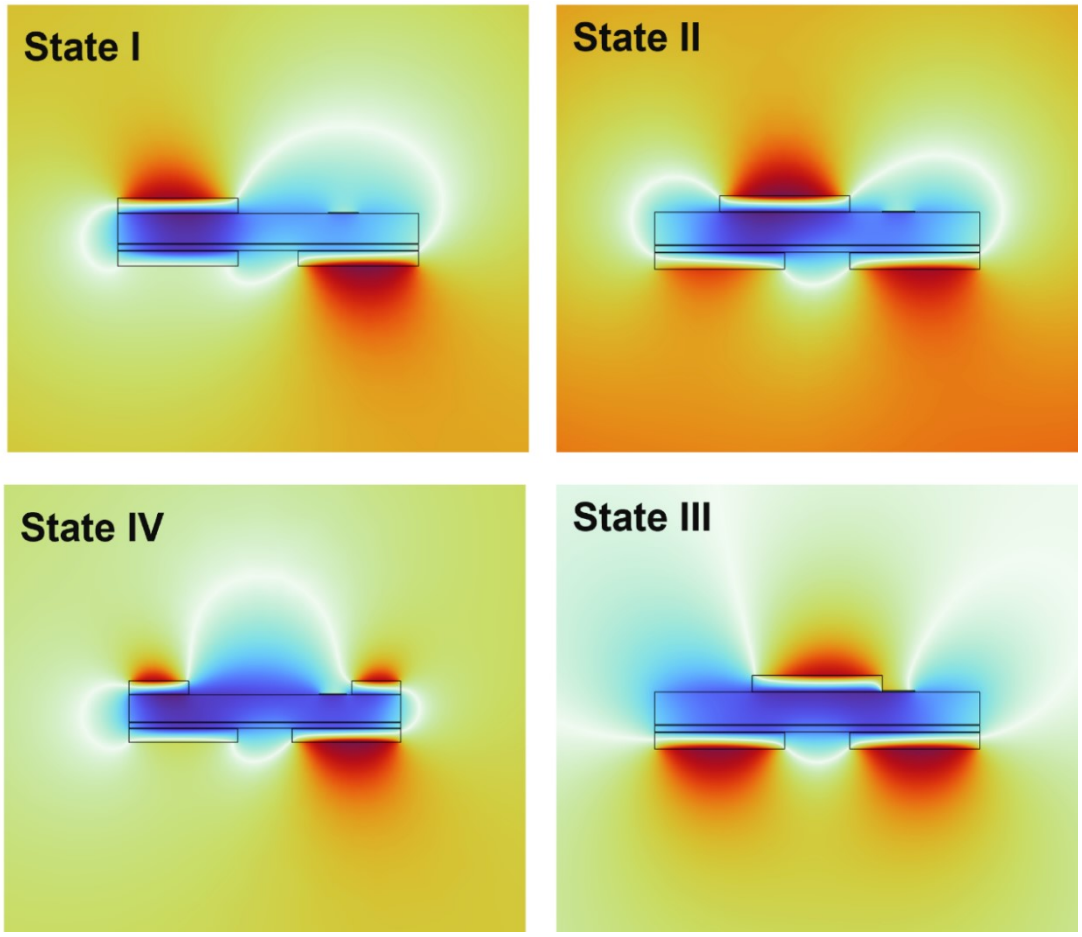

Figure. S5. Simulation of HEEH under different states.

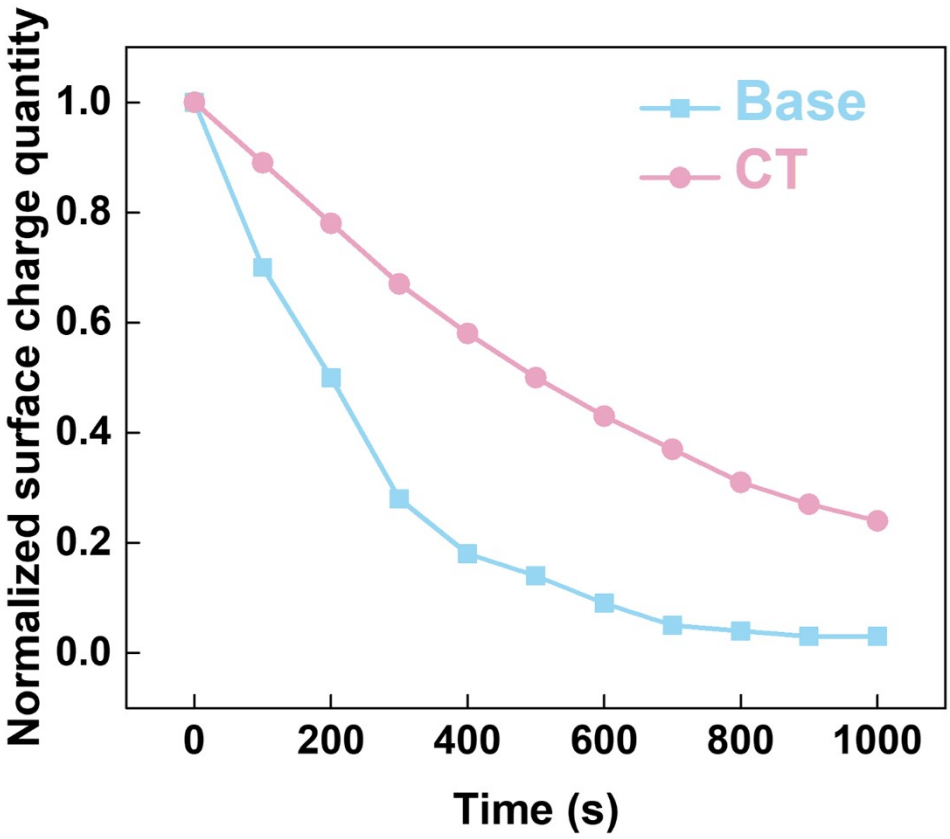

Figure. S6. Surface charge decay of the devices with and without the charge trapping layer.

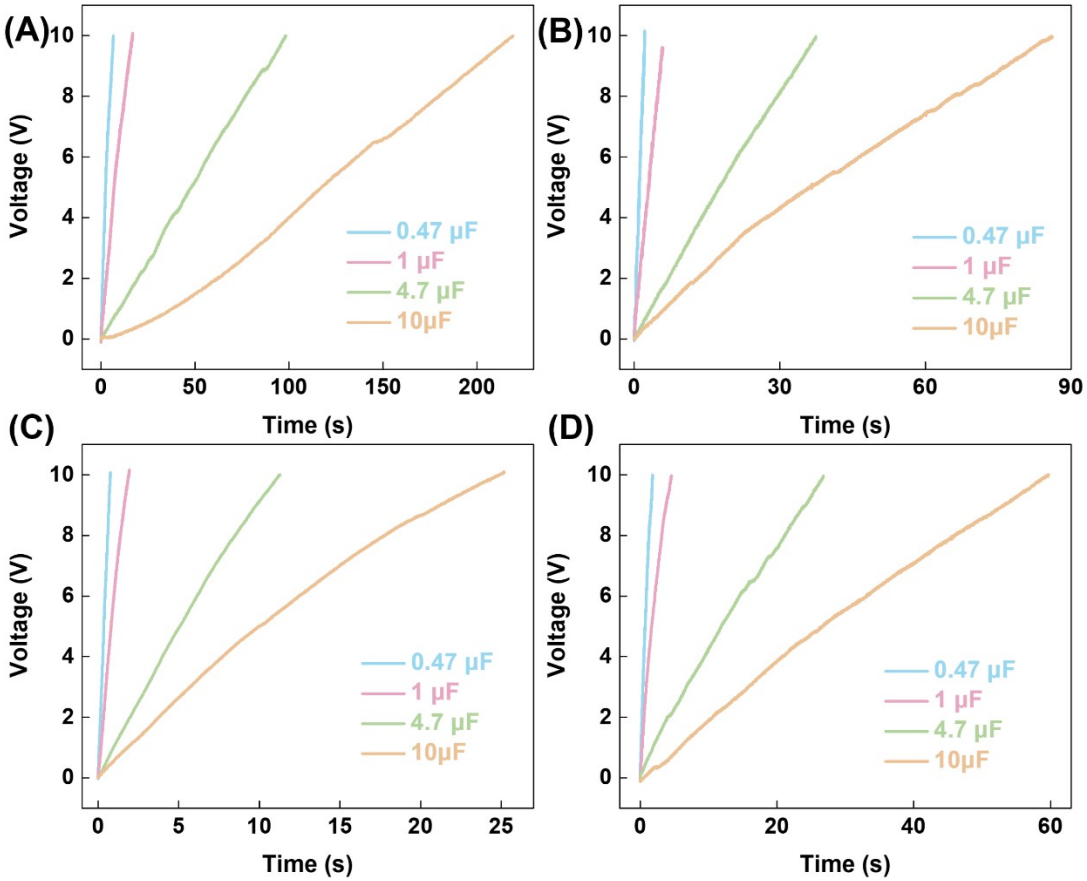

Figure. S7. Capacitor charging of base (A), CT (B), SC (C), and CT&SC (D) devices.

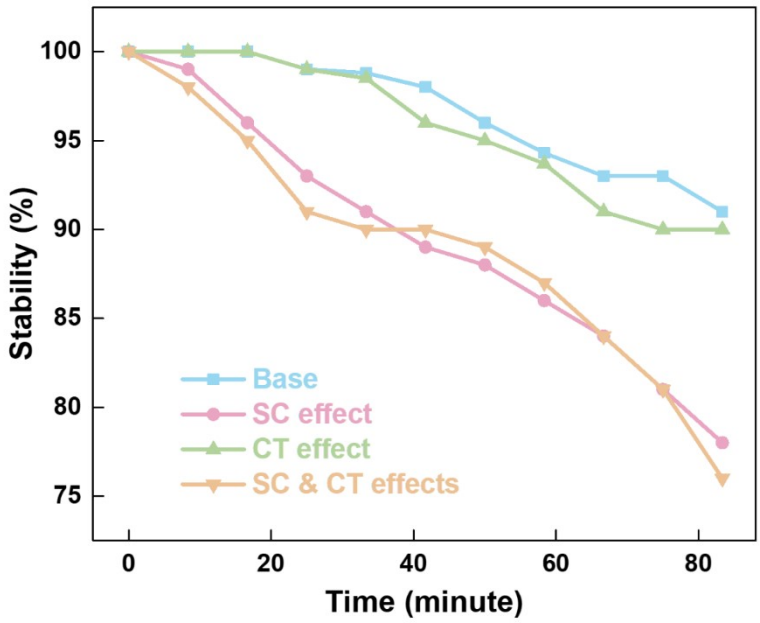

Figure. S8. Stability comparison of the devices.

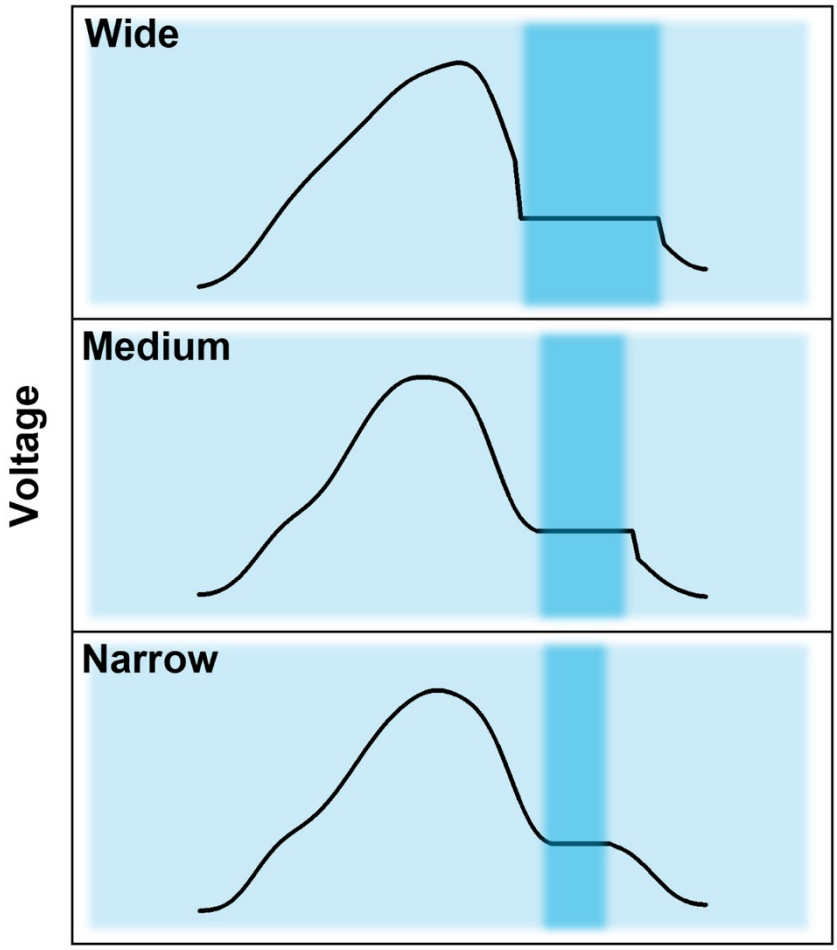

Figure. S9. Relationship between the width and duration of the short circuit contact.

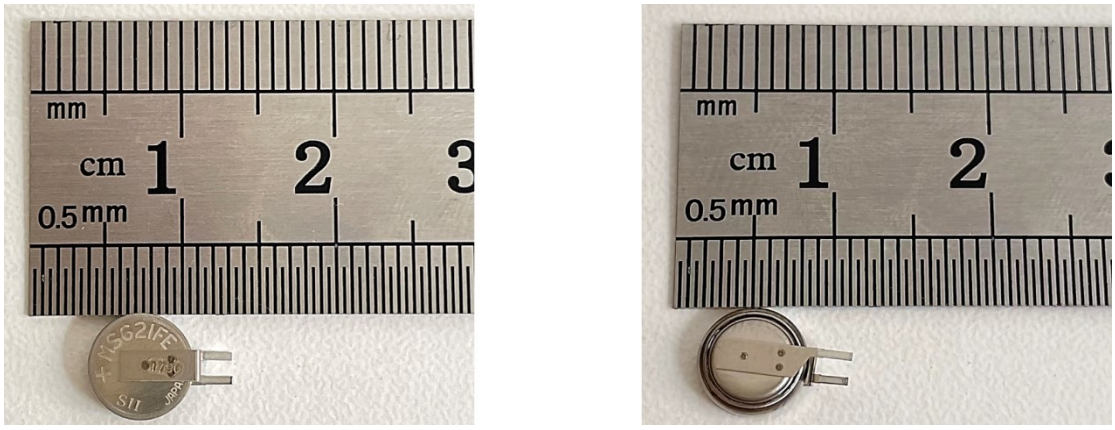

Figure. S10. Photograph of the commercial lithium battery.

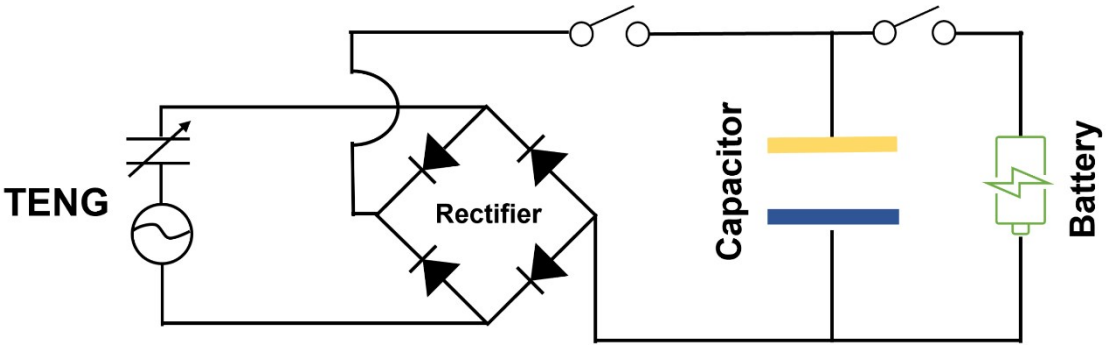

Figure. S11. Traditional circuit for capacitor and battery charging.

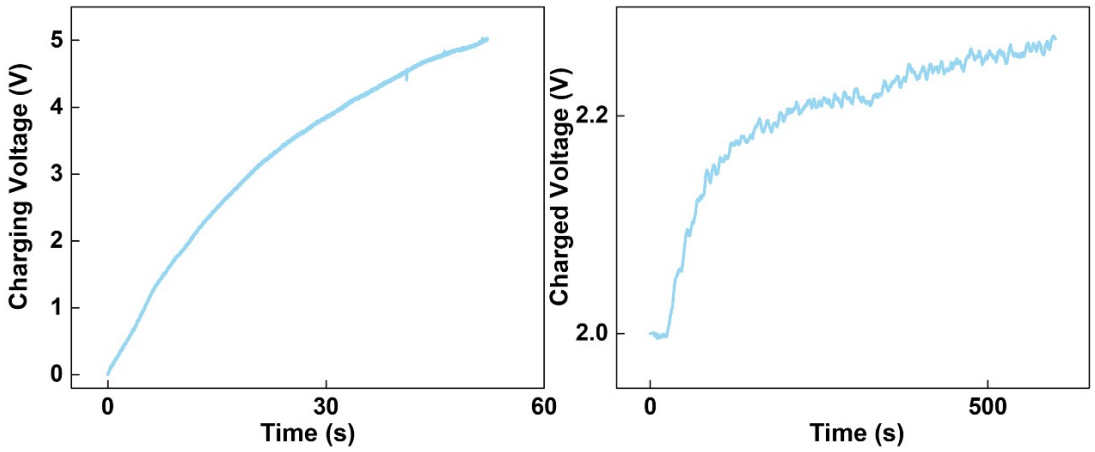

Figure. S12. Capacitor and battery charging with the traditional circuit design at rotation speed of 300 rpm.

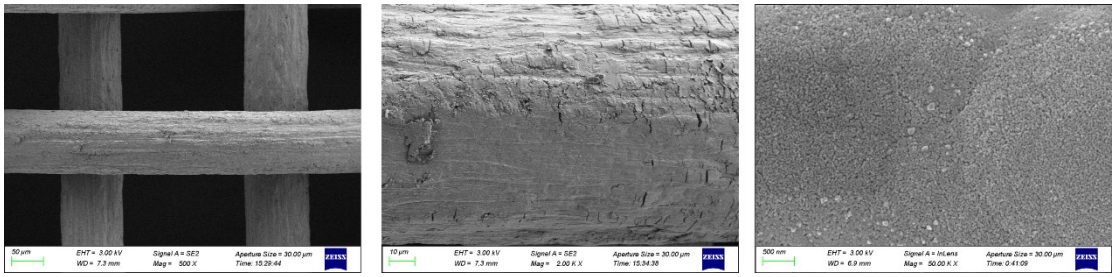

Figure. S13. SEM images of Mn_3O_4 nanoparticles-loaded titanium mesh.

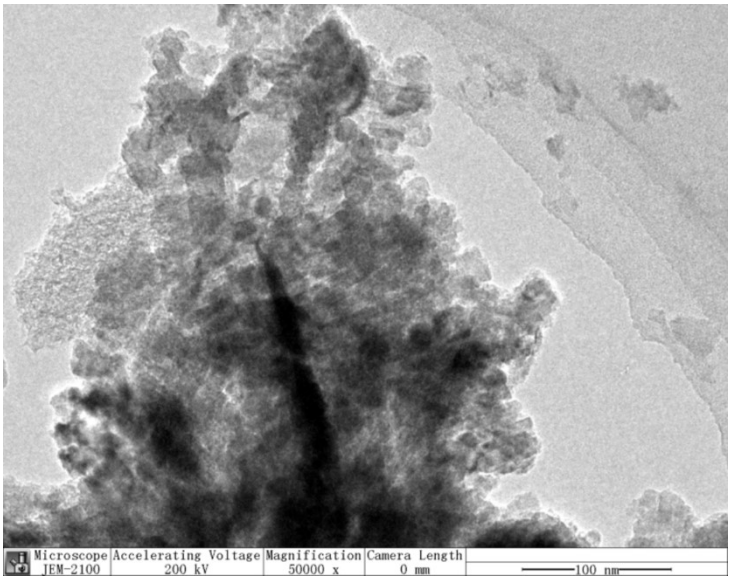

Figure. S14. TEM image of Mn_3O_4 nanoparticles.

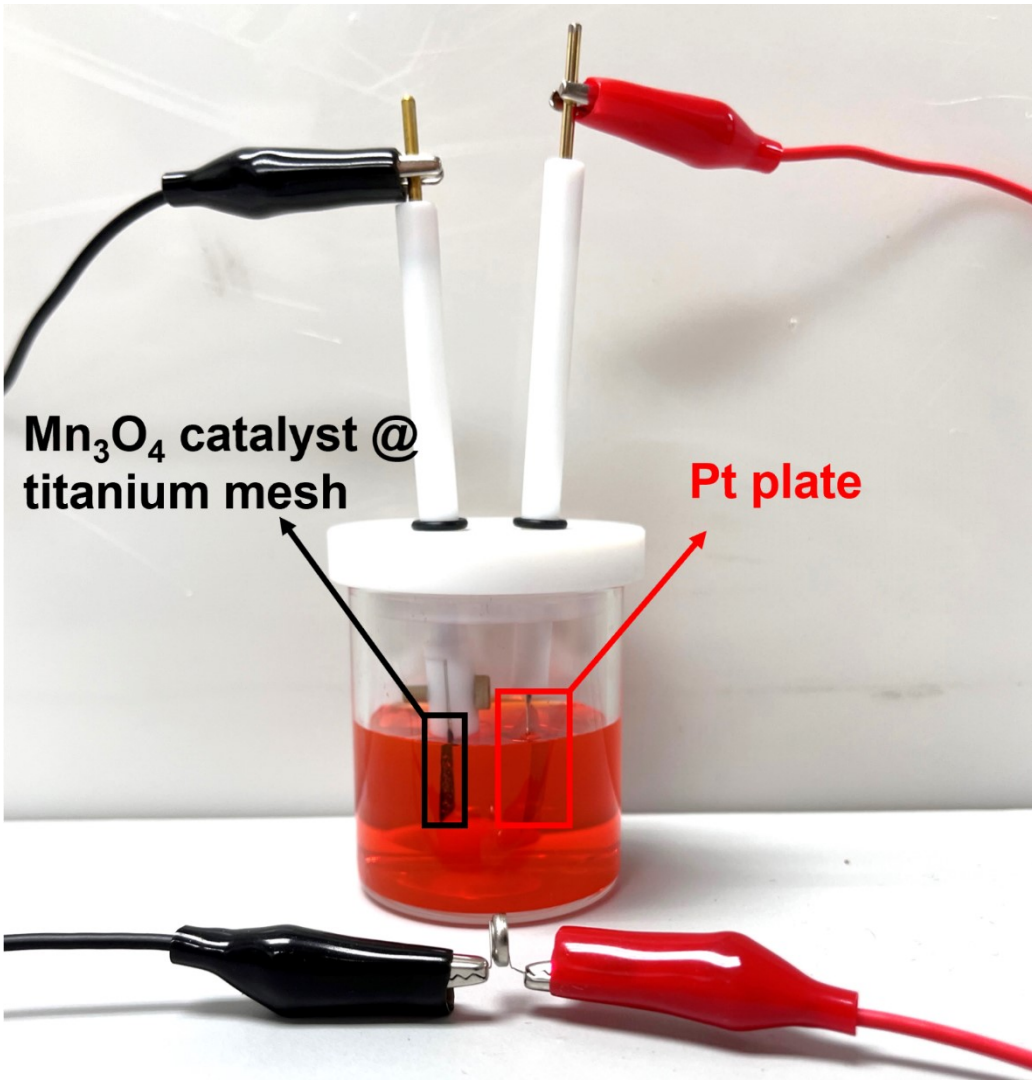

Figure. S15. Photograph of the wastewater treatment setup.

Table S1. Original and normalized radar chart.

Parameters \ Devices		Base	SC effect	CT effect	SC&CT effects
Origin indices	$\sigma(mC/m^2)$	152	348	280	661
	$P_{eff}(W/m^2)$	0.34	0.86	1.24	2.9
	$R_{int}(M\Omega)$	90	13	75	13
	Cost (HKD)	4.2	4.21	5.95	5.96
	$\rho(\%)$	91	78	90	76
Normalized indices	σ^*	0.23	0.53	0.42	1
	P_{eff}^*	0.12	0.3	0.43	1
	R_{int}^*	0.14	1	0.17	1
	$Cost^*$	0.7	0.71	0.99	1
	ρ^*	1	0.86	0.99	0.83

Table S2. Performance comparison with prominent rotary-structured devices.

Original power density & impedance		Device Diameter (mm) & Number of the electrode baldes		Standardized power density	Reference	Strategy	Barrier(s)
2.9 W/m^2 960 W/m^3 (150 rpm)	**10 MΩ**	**100**	**8**	**1.16 W/m^2/Hz 384 W/m^3/Hz**	**This Work**	**Charge trapping and short-circuiting effect**	**Abrasion (to be resolved with non-contact/ soft contact)**
2.032 W/m^2 ~203.2 W/m^3 (240 rpm)	10 MΩ	150	12	1.3 W/m^2/Hz 130 W/m^3/Hz	S2	phase-shift design	Difficult to replicate the phase-shift design on different devices
2.53 W/m^2 ~316 W/m^3 (150 rpm)	660 MΩ	100	8	1 W/m^2/Hz 126 W/m^3/Hz	S3	Ternary Dielectric Triboelectrification Effect	Complex fabrication process
5.74 W/m^2 ~382 W/m^3 (60 rpm)	30 MΩ	90	10	5.74 W/m^2/Hz 382 W/m^3/Hz	S4	capture dissipation charge	Suspended electrodes are hard to locate
1.4 W/m^2 ~140 W/m^3 (60 rpm)	200 MΩ	120	4	1.4 W/m^2/Hz 140 W/m^3/Hz	S5	Automatic Mode Switching and Charge Excitation	Sophisticated structure of centrifugal driving layer
1 W/m^2 ~227 W/m^3 (300 rpm)	30 MΩ	210	6	0.2 W/m^2/Hz 45.4 W/m^3/Hz	S6	self-excited amplification	Pre-friction before use Introducing of voltage-multiplying circuit
5.32 W/m^2 ~532 W/m^3 (600 rpm)	110 MΩ	221	4	0.532 W/m^2/Hz 53.2 W/m^3/Hz	S7	ternary dielectric triboelectrification	Complex fabrication process
3.45 W/m^2 ~345 W/m^3 (60 rpm)	5 MΩ	90	48	3.45 W/m^2/Hz 345 W/m^3/Hz	S8	Interface Liquid Lubrication	Drying of liquid lubricants
0.65 W/m^2 ~124 W/m^3 (90 rpm)	5 GΩ	230	12	0.43 W/m^2/Hz 82.6 W/m^3/Hz	S9	charge accumulation	Optimum electrode division scheme for different designs
1.15 W/m^2 ~164 W/m^3 (60 rpm)	25 MΩ	100	8	1.15 W/m^2/Hz 164 W/m^3/Hz	S10	charge space-accumulation	Sophisticated 3D structural design
0.32 W/m^2 ~50 W/m^3 (600 rpm)	100 MΩ	200	45	0.032 W/m^2/Hz 5 W/m^3/Hz	S11	electrostatic breakdown	charge collecting electrode is hard to locate

References

1. S. Niu and Z. L. Wang, *Nano Energy*., 2015, **14**, 161-192.
2. P. Chen, J. An, R. Cheng, S. Shu, A. Berbille, T. Jiang and Z.L. Wang, *Energy Environ. Sci*., 2021, **14**, 4523-4532.
3. Q. Li, Y. Hu, Q. Yang, X. Li, X. Zhang, H. Yang, P. Ji, Y. Xi and Z.L. Wang, *Adv. Energy Mater*., 2022, **13**, 2202921.
4. W. He, C. Shan, H. Wu, S. Fu, Q. Li, G. Li, X. Zhang, Y. Du, J. Wang, X. Wang and C. Hu, *Adv. Energy Mater*., 2022, **12**, 2201454.
5. S. Fu, W. He, Q. Tang, Z. Wang, W. Liu, Q. Li, C. Shan, L. Long, C. Hu and H. Liu, *Adv. Mater*., 2022, **34**, e2105882.
6. L. Long, W. Liu, Z. Wang, W. He, G. Li, Q. Tang, H. Guo, X. Pu, Y. Liu and C. Hu, *Nat. Commun*., 2021, **12**, 4689.
7. Q. Li, W. Liu, H. Yang, W. He, L. Long, M. Wu, X. Zhang, Y. Xi, C. Hu and Z.L. Wang, *Nano Energy*., 2021, **90**, 106585.
8. L. Zhou, D. Liu, Z. Zhao, S. Li, Y. Liu, L. Liu, Y. Gao, Z.L and Wang, J. Wang, *Adv. Energy Mater*., 2020, **10**, 2002920.
9. R. Lei, Y. Shi, Y. Ding, J. Nie, S. Li, F. Wang, H. Zhai, X. Chen and Z.L. Wang, *Energy Environ. Sci*., 2020, **13**, 2178-2190.
10. W. He, W. Liu, J. Chen, Z. Wang, Y. Liu, X Pu, H. Yang, Q. Tang, H. Yang, H. Guo and C. Hu, *Nat. Commun*., 2020, **11**, 4277.
11. D. Liu, X .Yin, H. Guo, L. Zhou, X. Li, C. Zhang, J and Wang, Z.L. Wang, *Sci. Adv*., 2019, **5**, eaav6437.